IN-SITU STUDY OF MATERIALS TRANSFORMATION

In situ ion irradiation of amorphous TiO$_2$ nanotubes

Chao Yang[1], Tristan Olsen[2], Miu Lun Lau[3], Kassiopeia A. Smith[4], Khalid Hattar[5], Amrita Sen[1], Yaqiao Wu[2,6], Dewen Hou[2], Badri Narayanan[7], Min Long[3], Janelle P. Wharry[1,a)], Hui Xiong[2,6,a)] (ORCID)

[1] School of Materials Engineering, Purdue University, 205 Gates Road, West Lafayette, IN 47906, USA
[2] Micron School of Materials Science & Engineering, Boise State University, 1910 University Drive, Boise, ID 83725, USA
[3] Department of Computer Science, Boise State University, 1910 University Drive, Boise, ID 83725, USA
[4] Fifth Gait Technologies, Colorado Springs, CO 80919, USA
[5] Sandia National Laboratories, Albuquerque, NM 87185, USA
[6] Center for Advanced Energy Studies, 995 MK Simpson Blvd, Idaho Falls, ID 83401, USA
[7] Department of Mechanical Engineering, University of Louisville, 332 Eastern Parkway, Louisville, KY 40292, USA
a) Address all correspondence to these authors. e-mails: jwharry@purdue.edu; clairexiong@boisestate.edu

Understanding of structural and morphological evolution in nanomaterials is critical in tailoring their functionality for applications such as energy conversion and storage. Here, we examine irradiation effects on the morphology and structure of amorphous TiO$_2$ nanotubes in comparison with their crystalline counterpart, anatase TiO$_2$ nanotubes, using high-resolution transmission electron microscopy (TEM), in situ ion irradiation TEM, and molecular dynamics (MD) simulations. Anatase TiO$_2$ nanotubes exhibit morphological and structural stability under irradiation due to their high concentration of grain boundaries and surfaces as defect sinks. On the other hand, amorphous TiO$_2$ nanotubes undergo irradiation-induced crystallization, with some tubes remaining only partially crystallized. The partially crystalline tubes bend due to internal stresses associated with densification during crystallization as suggested by MD calculations. These results present a novel irradiation-based pathway for potentially tuning structure and morphology of energy storage materials.

Introduction

Titanium dioxide (TiO$_2$) has attracted intensive research interest in a variety of fields due to its outstanding properties such as high dielectric constant, high chemical stability, and high refractive index [1–5]. Nanostructuring of TiO$_2$ has further led to enhanced performance by increasing the surface-to-volume ratio [6–10]. For example, TiO$_2$ nanotubes (TiO$_2$-NT) demonstrate enhanced electrochemical properties as a negative electrode material for rechargeable lithium ion batteries, compared to its bulk TiO$_2$ counterpart [10]. Research [11–29] has shown that the morphology of TiO$_2$-NT can greatly alter its properties, and researchers have attempted to modify the morphology of TiO$_2$-NT through various approaches such as controlling time and washing treatment in hydrothermal synthesis [30], or electrolyte concentration and water content in electrochemical anodization synthesis [31].

It is well established that ion irradiation introduces defects and regional lattice disorder in solid materials [32]. Theoretical studies of proton irradiation in TiO$_2$ have shown that grain boundaries in both anatase and rutile polymorphs act as sinks for irradiation-induced point defects [33, 34]. Nanostructured crystalline TiO$_2$ has a large volume fraction of surfaces and grain boundaries, which may contribute to a higher resistance to radiation damage. Previous studies have shown that proton irradiation improves the electrochemical performance of both amorphous and anatase TiO$_2$-NTs by creating point defects and extended defects while maintaining the original morphology [35, 36]. Nevertheless, limited work has investigated the morphological changes of TiO$_2$-NTs in response to heavy ion irradiation, even though ion beam modification is an effective means of nanomaterial synthesis [37] and morphological tailoring of one-dimensional nanomaterials such as carbon nanotubes [38–40], as well as some two-dimensional nanomaterials [41, 42]. Ion irradiation damage is initiated through a flux of energetic particles, leading to the displacement of atoms within a target material. Ion irradiation affects the material by transferring

energy from the incident projectile to the solid, either through electronic or nuclear stopping [43]. The atomic structures of metal oxide ceramics are complex [44], leading to a variety of atomic processes under irradiation that are not thoroughly understood.

Herein, we report a transmission electron microscopy (TEM) in situ Au⁻ ion irradiation study in which we monitor the ion irradiation-induced morphological and structural changes in amorphous and anatase TiO_2-NTs. Post-irradiation high-resolution TEM (HRTEM) characterization reveals irradiation-induced amorphous-to-crystalline transformations. Complementary molecular dynamics (MD) simulations confirm that these irradiation-induced phase transformations have significant implications on the overall structure and morphology of initially amorphous TiO_2-NTs. This work helps to fill the knowledge gap of how ion irradiation affects the morphology of TiO_2-NTs and, more generally, provides insight into the potential applications of ion irradiation for tuning the morphological stability of one-dimensional ceramic nanomaterials.

Results

Irradiation-induced structural and morphological changes

A single nanotube in each specimen is tracked throughout the in situ irradiation via TEM. Figure 1 shows still frames from TEM videos (complete videos are available in the Supplementary Information) demonstrating the behavior of an amorphous and an anatase TiO_2 nanotube under Au⁻ ion in situ irradiation. Both tubes are initially straight with wall thickness of ~ 10 nm

and outer diameter ~ 60 nm, which are consistent with their dimensions previously confirmed by SEM and TEM [35]. Almost immediately upon irradiation, the amorphous nanotube begins to bend, and its radius of curvature continues to decrease over a duration of 80 s, until a relatively steady-state curvature is achieved. The nanotube wall thickness and outer diameter do not change appreciably during the irradiation-induced curvature. By contrast, the anatase TiO_2-NT is dimensionally and morphologically stable over the same irradiation period. While some changes in contrast (circled in Fig. 1b) are produced in the anatase nanotubes, these features are too small to resolve as defects or phase changes; these features do not appear to accumulate, and this is likely due to the high sink strength of the single-walled nanotube surface area [45, 46].

After in situ irradiation, lower magnification TEM imaging provides a general overview of the aggregate behavior of the amorphous and anatase TiO_2-NTs upon irradiation (Fig. 2). All tubes in the anatase TiO_2 specimen remain straight, and their dimensions appear unaffected by irradiation. Meanwhile only ~ 15% of the amorphous tubes are bent like the individual tube tracked during in situ irradiation (highlighted with red ovals in Fig. 2a). There is no apparent correlation between amorphous nanotube length or position, and the tendency to exhibit irradiation-induced curvature. It should also be noted that the curved nanotubes do not have an obvious bending preference, neither concentrically nor toward a specific direction.

HRTEM at various positions along the length of the amorphous nanotubes post-irradiation provides further insight into the mode of curvature. We look first at a typical straight tube in the amorphous sample after irradiation, Fig. 3a. Selected points
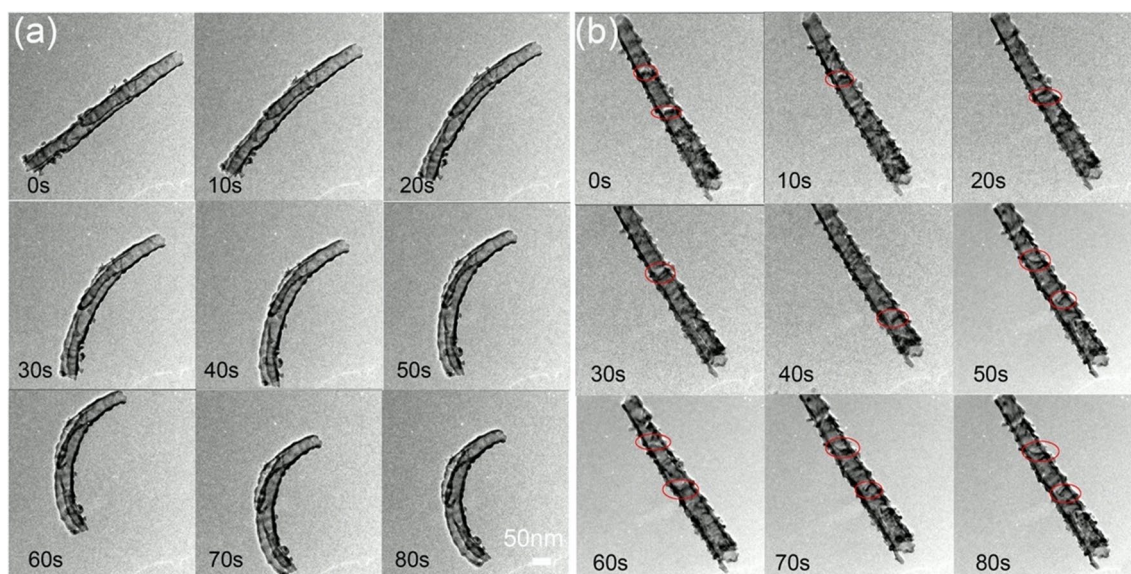

Figure 1: TEM still frames taken at 10 s intervals from 0 to 80 s, showing behavior of an (a) amorphous and (b) anatase TiO_2 nanotube under in situ 46 keV Au⁻ ion irradiation.
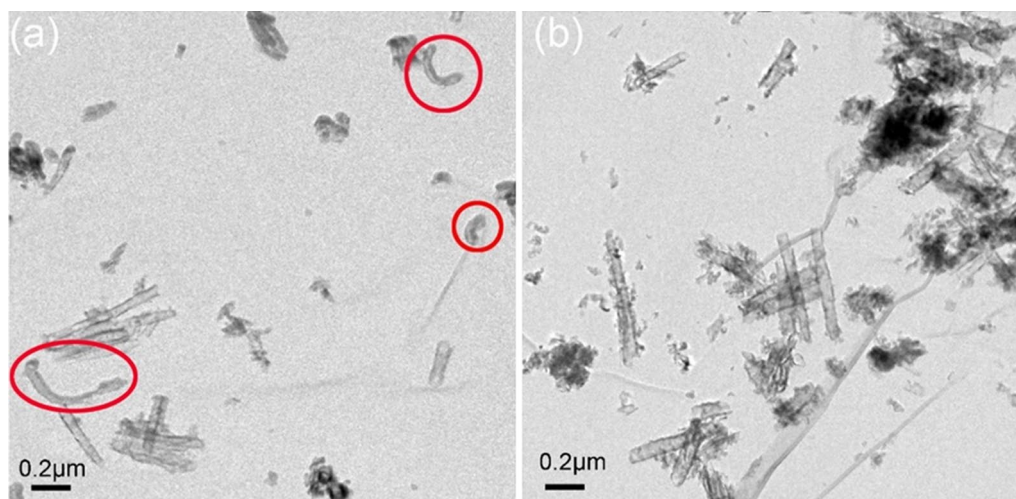
Figure 2: Bright-field TEM image of (a) amorphous and (b) anatase TiO$_2$ nanotubes after irradiation, with irradiation-induced nanotube curvature circled.

of examination along the nanotube are labeled, and their corresponding HRTEM images are provided in Fig. 3b–j; insets provide fast Fourier transforms (FFTs) and enlarged HRTEM images of the white-framed regions to show the lattice spacing. The tube is fully crystallized at all points examined along the nanotube. Although crystal structure cannot be definitively confirmed through HRTEM lattice spacing, the interplanar distance is 3.52 Å, which is at least consistent with the (101) plane of anatase TiO$_2$. Additional TEM images of straight tube in the amorphous sample after irradiation are provided in Figure S3 (Supplementary Information), revealing that the amorphous tubes consistently exhibit irradiation-induced crystallization.

A typical curved tube in the amorphous sample after irradiation is shown in Fig. 4a, with selected points of examination labeled, and their corresponding HRTEM images are provided in Fig. 4b–k. The portion of the tube that remains straight (i.e., regions b–e) is still amorphous. However, the curved portion of the tube (i.e., regions f–k) has partially crystallized into nanosized crystalline regions, encircled by white-dashed lines. The interplanar distance measured from the HRTEM images indicates that the majority of the nanocrystals may be anatase, with interplanar distance of 3.52 Å for (101) planes and 2.43 Å for (103) planes, all identified in white (Fig. 4f, g, i, k). A small portion of nanocrystals may be rutile, with interplanar distance of 3.25 Å for (110) planes, marked in green (Fig. 4h, j). Additional TEM images of curved tubes in the amorphous specimen after irradiation are provided in Figures S4–S5 (Supplementary Information), confirming that the curved nanotubes retain amorphous regions that remain straight, and their curved regions are partially crystallized.

Volume calculations

Figure 5 shows snapshots of the classical molecular dynamics (CMD) simulations of equilibrized anatase and amorphous TiO$_2$. The results show that the equilibrized anatase TiO$_2$ has a cell volume of 72.6×10^6 Å^3 at 300 K (cell dimensions 526.8 Å $\times$ 476.1 Å $\times$ 271.9 Å). Meanwhile, the amorphous TiO$_2$ cell volume is 116.7×10^6 Å^3 at 300 K (cell dimensions 632.9 Å $\times$ 573.9 Å $\times$ 321.4 Å). This represents a 60% volume increase from anatase to amorphous at the same conditions. The result is consistent with experimental findings considering the atoms in an amorphous phase are not closely packed, with considerable free volume existing between atoms.

Discussion

Irradiation-induced crystallization

Ion and electron irradiation have been shown to generate highly localized nanocrystalline domains (~ 10 nm) in amorphous materials in 10–100 s of seconds [47–50]. The nanocrystallites observed in the curved nanotubes are consistent with these reports. Qin et al. [51] present a foundational theory on the mechanism of irradiation-induced nucleation of nanocrystallites in an amorphous material that involves a competition between energy injection and export. This mechanism is in contrast to the classical nucleation theory, which simply involves minimization of the Gibbs free energy. Qin's theory states that irradiating particles *inject* a total energy, ΔE_{n}, into the material, which is dissipated through

$$\Delta E_{\mathrm{n}} = \Delta E_{\mathrm{dis}} + \Delta E_{\mathrm{sto}}, \tag{1}$$
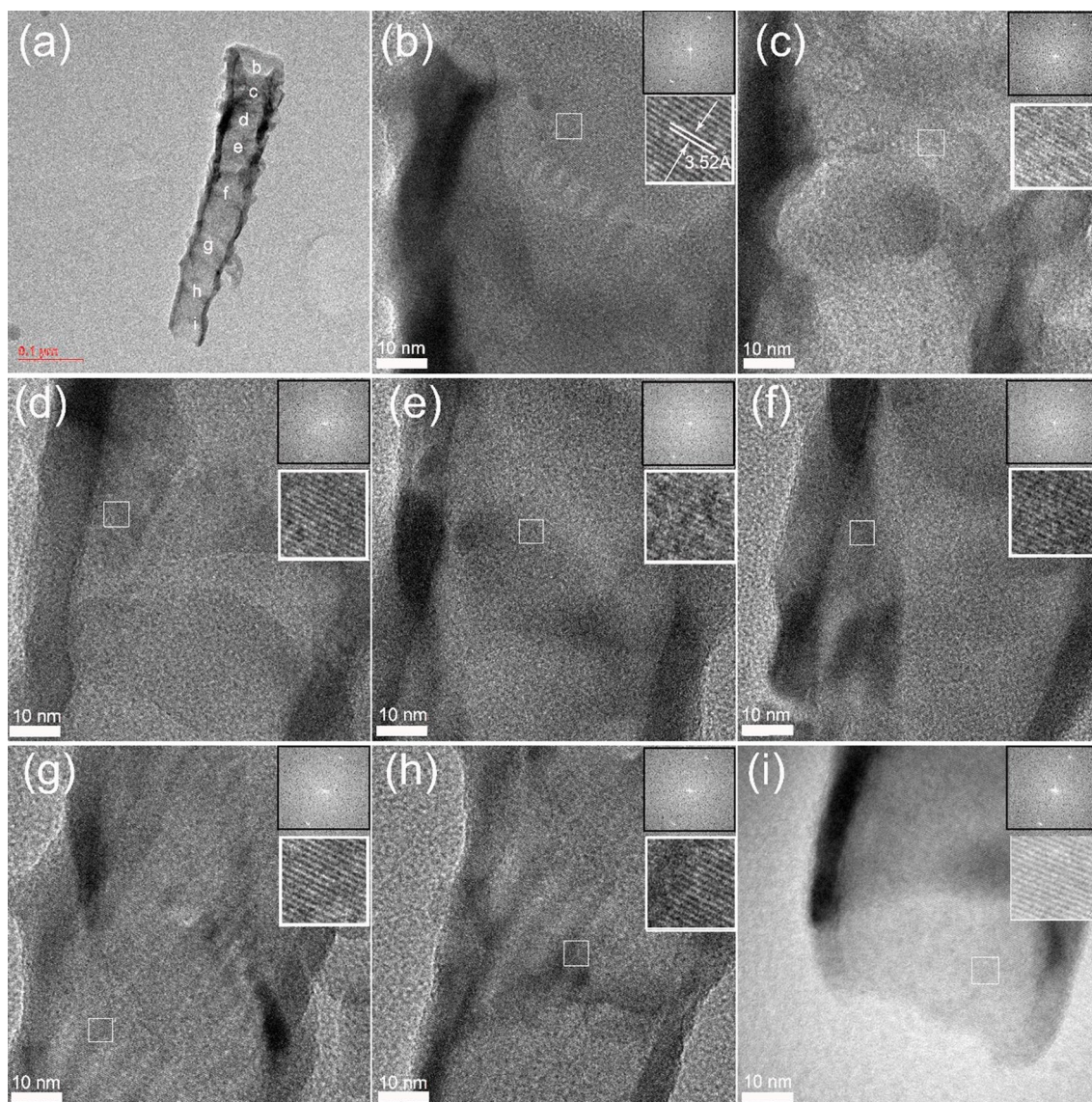
Figure 3: (a) TEM image of a typical straight tube in amorphous sample after irradiation, (b)–(f) HRTEM images corresponding to labels b-f marked in (a). Insets on HRTEM images show FFT and high magnification lattice structure of the white boxed regions, which reveal irradiation-induced amorphous-to-anatase crystallization.

where ΔE_{dis} is the energy released to the environment by atomic rearrangement and ΔE_{sto} is the energy stored as point defects that create additional disorder in the system. But at the same time, the original amorphous phase is a high-energy metastable state, which will *export* energy as the atoms will tend to rearrange into a lower-energy (i.e., crystalline) configuration. This crystalline ordering will tend to occur during the time intervals between the arrivals of two successive irradiating particles and will occur through thermal conduction from the irradiated region to the surrounding amorphous matrix. This exported energy, ΔE_{r} is

$$\Delta E_{\mathrm{r}} = \Delta E_{\mathrm{dis}} + \Delta E_{\mathrm{rea}}, \qquad (2)$$

where ΔE_{rea} is the difference in free energy between the original amorphous state and the post-rearrangement crystalline state. Thus, the total energy change in the irradiated region is $\Delta E_{\mathrm{t}} = -\Delta E_{\mathrm{r}} + \Delta E_{\mathrm{n}}$, in which the negative and positive terms represent energy export and injection, respectively. Crystallization will occur if sufficient numbers of atoms rearrange themselves during irradiation, such that energy export exceeds energy injection, according to the inequality:

$$\Delta E_{\mathrm{r}} > \Delta E_{\mathrm{n}} \text{ , i.e., } \Delta E_{\mathrm{rea}} > \Delta E_{\mathrm{sto}}. \qquad (3)$$

By virtue of the tube nanostructure, the large surface-area-to-volume ratio promotes enhanced defect annihilation at the amorphous nanotube surfaces, resulting in reduced defect
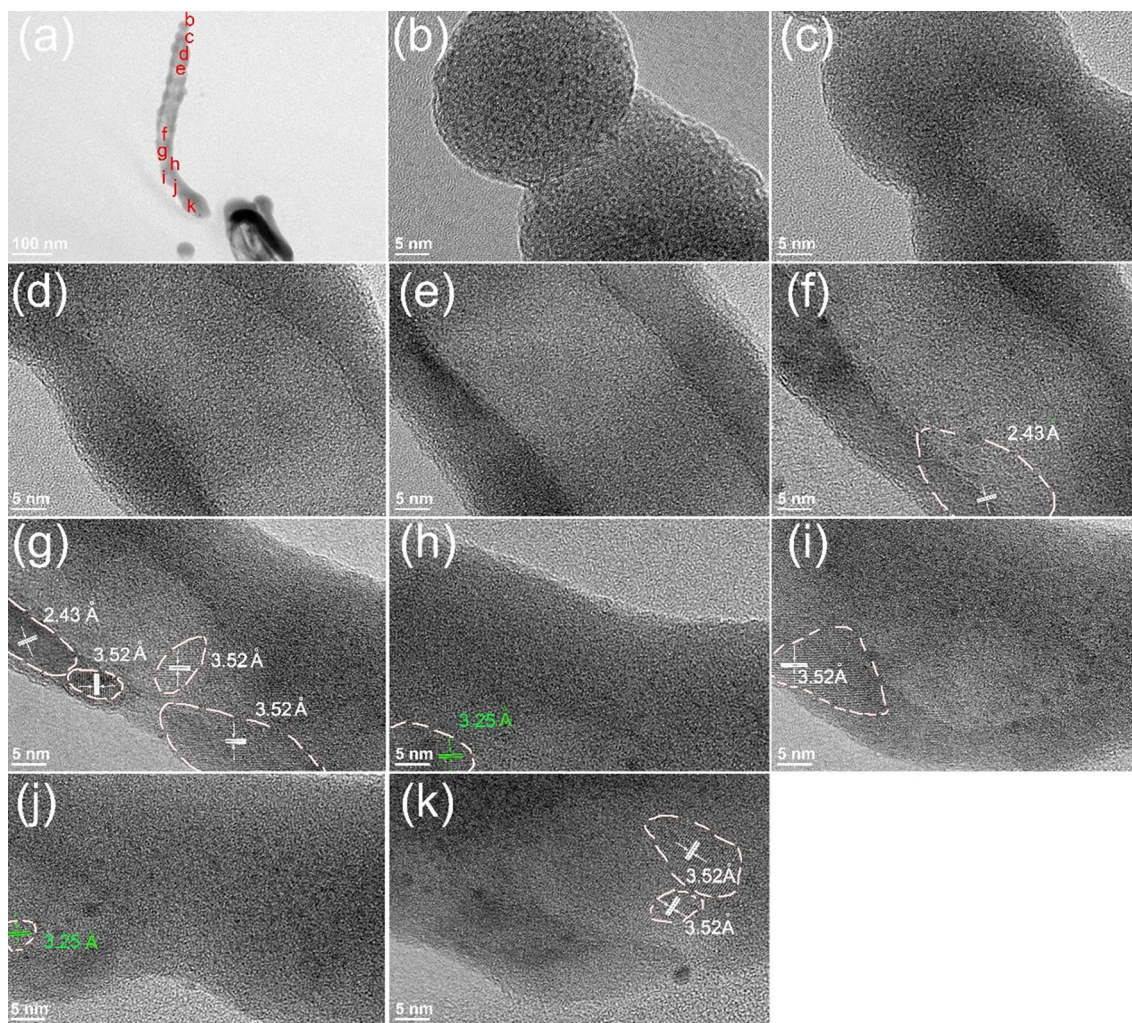
Figure 4: (a) TEM image of a typical curved tube in amorphous sample after irradiation, (b)–(k) HRTEM images corresponding to labels b–k marked in (a). HRTEM images show that the nanotube remains amorphous at positions (b)–(e) and undergoes partial crystallization at positions (f)–(k), with dashed lines encircling crystalline regions.
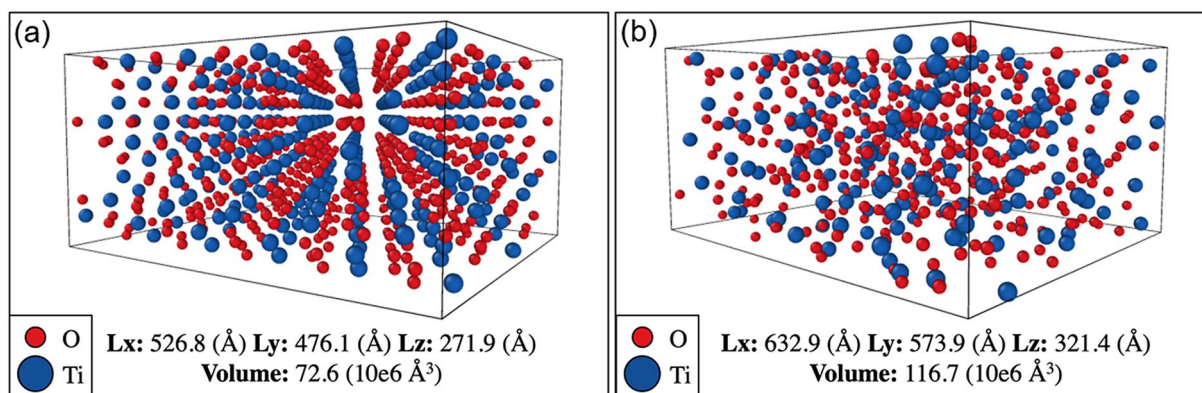

Figure 5: Comparisons of volume between (a) anatase and (b) amorphous TiO_2 in the CMD simulations at 300 K, with L_x, L_y, and L_z showing cell dimensions in the x-, y-, and z-directions.

storage in the tubes. Irradiation additionally increases atomic mobility in amorphous materials [52, 53], and thus, there is an even greater likelihood of energy dissipation. Hence, the inequality tends toward $\Delta E_{rea} \gg \Delta E_{sto}$, which can explain the predominant behavior of complete crystallization.

In order to explain the heterogeneous behavior in which some of the amorphous nanotubes form nanocrystalline domains (rather than complete crystallization), one must also account for the ion implantation profiles (i.e., ion range) and the energy loss mechanisms.

Ions incident on a target material lose energy along a continuum through nuclear stopping and electronic stopping [43, 54]. Nuclear stopping [55] involves direct ion-atom collisions and is understood through the binary collision approximation, in which a displacement cascade is generated and produces the Frenkel type defects in ceramics. On the other hand, electronic stopping [56] involves inelastic collisions between the incident ion and valence electrons in the target material, resulting in excitation of the incident and target ions. Electronic stopping is typically understood through two models: the Coulomb explosion model [57, 58] or the inelastic thermal spike model [54, 59]. Electrostatic potential energy generated by ionizations along the ion trajectory is converted: in the former model, to atomic kinetic energy, and in the latter model, converted through electron–phonon coupling to effectively produce local heating along the ion trajectory. The extent of irradiation-induced crystallization—and the size of nanocrystallites formed—decreases with increasing electronic stopping [60, 61]. Thus, partial crystallization may occur when the ions incident on a given nanotube primarily undergo electronic energy losses. The SRIM simulation for Au⁻ ions incident on TiO_2 shows that nuclear stopping is approximately an order of magnitude greater than electronic stopping at the irradiation energy of 46 keV, Fig. 6. This predominance of nuclear stopping, which generates sufficient

rearrangements to satisfy the inequality in Eq. (3), produces the majority of fully crystallized nanotubes, while fewer partially crystallized nanotubes form through electronic stopping. Alternatively, because the nanotubes are randomly dispersed onto the carbon TEM grid, they are randomly oriented relative to the incident ion beam.

The SRIM simulation shows that the 46 keV Au⁻ ion implantation peak in amorphous TiO_2 is located near 30 nm, Fig. 7. Since nanotube wall thickness is ~ 10 nm, many of the incident ions will completely pass through the target if the angle of incidence is normal to the lateral direction of the nanotube. Such a configuration would inherently limit the extent of nanocrystallite formation and could thus explain the partial crystallization of some tubes.

Nanotube bending mechanism

Stress is needed for any solid-state material to deform. As shown in Figs. 3 and 4, curved tubes have partially crystallized under irradiation, while straight tubes are fully crystallized from the initially amorphous phase. Thus, the bending likely occurs due to internal stresses generated during irradiation-induced partial crystallization in the amorphous tubes. This is supported by the MD volume calculations which confirm that significant densification (i.e., volume decrease) occurs during the amorphous-to-crystalline transformation. If the irradiation-induced crystallization occurs unevenly or heterogeneously—as in the partially crystallized nanotubes—internal stress can build up as different regions of the nanotube densify to differing extents. Consequently, sufficient torque can build up in the middle (lengthwise) of the tubes so as to induce bending into a "C"-shape (the crystallization-induced internal stresses are more easily relaxed near the free ends of the nanotube; thus, the bending
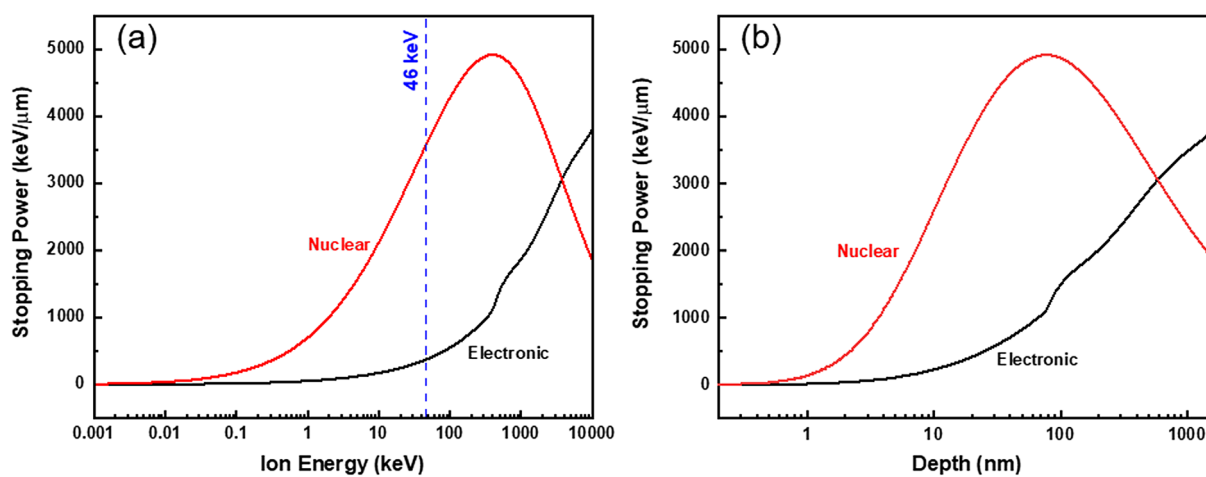

Figure 6: Electronic and nuclear stopping power for Au ions in anatase TiO_2 as a function of (a) ion energy and (b) ion target depth.
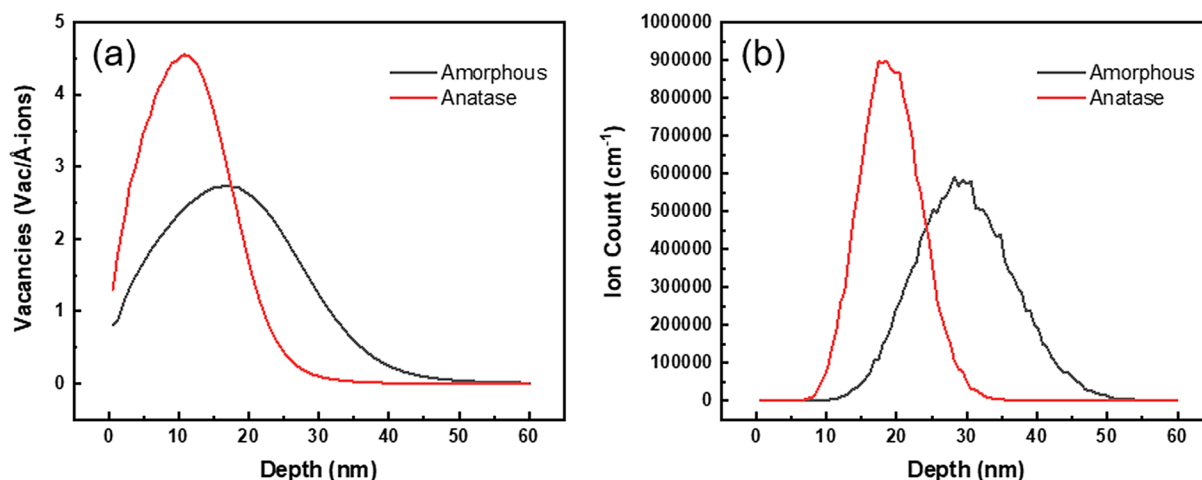
Figure 7: Comparison of (a) vacancy production and (b) ion implantation distributions for 46 keV Au⁻ ions in amorphous and anatase TiO$_2$ as calculated using SRIM in detailed calculation mode with full damage cascades.

is confined to the central region along the length of the tubes). The amorphous nanotubes that experience complete crystallization are not bent, because they lack amorphous-crystalline interfaces where internal stresses would have arisen due to volume differences between the amorphous and crystalline phases.

Ion irradiation-induced densification is a well-known phenomenon that has been observed principally in oxide ceramics, as well as other ceramic [62] and metallic [63, 64] materials. This densification is sometimes associated with deformation, as in work from Snoeks et al. [65], who conducted a 4 MeV Xe^{4+} ion irradiation on amorphous silica (SiO$_2$) thin films containing 5 μm trenches. Their trenches exhibited dramatic macroscopic contraction in the direction of the ion beam, and expansion perpendicular to the ion beam; these deformations did not saturate with irradiation fluence. This deformation–densification mechanism has been attributed to local heating and thermal expansion around ion tracks [65–67], similar to the established phenomenon of ion irradiation-induced deformation in glasses under extreme ion energies (~ 100s of MeV) [68]. Alternatively, irradiation-enhanced Newtonian plastic shear flow associated with local melting [69] has also been suggested as a mechanism for stress relaxation that can generate macroscopic deformations. However, materials that undergo ion irradiation-induced densification—namely, amorphous silica [65–67] and amorphous hydroxyapatite thin films [62]—remain amorphous even upon densification. Although the crystal structures of TiO$_2$ differ from those observed to densify under ion irradiation, there is nevertheless support for a novel ion irradiation-induced densification mechanism via phase transformation (i.e., crystallization) observed herein.

Most similar to the phase transformation mechanism in the present study may be the electron irradiation-induced densification study in silica glass from Buscarino et al. [70]. They observed polyamorphic transformations under electron irradiation, which were associated with the nucleation of localized regions containing high defect concentration and high density, dispersed throughout the material volume. Nevertheless, the irradiating particle—i.e., electrons—cannot alone explain the transformations, as other reports show that electron irradiation does not induce phase transformations in amorphous silica [70, 71] and amorphous silica nanoballs [72]. Finally, it is also worth noting that irradiation-enhanced densification has also been observed [73, 74] and modeled [75, 76] in crystalline UO$_2$ oxide nuclear fuel, generally under neutron irradiation. That mechanism is also unique: in UO$_2$, reduction of micro-macroscale porosity (associated with nuclear fission gas bubbles) occurs through a sintering and bubble-closure mechanism [75].

Other factors beyond phase transformation and atomic-level stresses may also influence the nanotube curvature observed in this study. Physical constraints from surrounding nanotubes within a cluster of nanotubes could help maintain the structural integrity of a given nanotube, as previously suggested for proton irradiated anatase TiO$_2$ [35]. Additionally, the nanotubes are randomly scattered on a carbon membrane TEM grid. Differences in the amount and nature of the physical contact between a tube and the carbon membrane could lead to different thermal conduction behaviors. For example, tubes having greater contact area with the carbon membrane may be able to more effectively conduct heat (generated by the incident irradiation) away from the tube. Finally, the high surface energy of TiO$_2$-NTs may also contribute to the driving force for crystallization.

Conclusion

In situ TEM ion irradiation was carried out on amorphous and anatase TiO_2 nanotubes, with complementary molecular dynamics simulations to calculate the volume of amorphous and anatase TiO_2. Anatase TiO_2 nanotubes exhibit morphological stability throughout irradiation. Amorphous TiO_2 nanotubes undergo irradiation-induced crystallization. While the majority of the initially amorphous tubes become fully crystallized, some tubes remain only partially crystallized. These partially crystalline tubes also bend during irradiation, due to internal stresses associated with the densification that occurs through crystallization, as confirmed by MD calculations. This mechanism presents a novel irradiation-based pathway for tuning the structure and morphology of advanced energy storage anode materials.

Methods

Materials

The TiO_2 nanotubes were synthesized by electrochemical anodization; details of this process can be found in previous works [35, 36]. In brief, pure titanium foil (0.127 mm, 99.8%, Alfa Aesar) was electropolished [77], followed by a three-step sonication cleaning in acetone, isopropanol, and deionized (DI) water each for 5 min. The anodization was done in a two-electrode cell with Ti foil as the working electrode and a Pt mesh as the counter and reference electrode. The back of the Ti foil was covered by protective tapes to ensure uniform current distribution. The anodization was carried out for 10 min under a constant voltage of 15 V in an electrolyte of 0.36 M ammonium fluoride (Aldrich) in 95 vol% formamide (Fisher) and 5 vol% DI water. The anodized specimens were then ultrasonically cleaned in DI water for 30 s. The as-prepared specimens were amorphous, as confirmed by X-ray diffraction (XRD) and TEM with selected area electron diffraction (SAED) shown in Figures S1 and S2, respectively (Supplementary Information). The crystalline specimens were prepared by annealing the as-prepared specimens in a mixture of 20% O_2 and 80% Ar at 450 °C for 4 h.

Irradiation and characterization

Both amorphous and anatase TiO_2 nanotube samples for in situ Au ion irradiation with TEM were prepared by scraping the nanotubes off the Ti substrates and then suspending them on carbon-stabilized formvar film 300 mesh TEM grids. In situ TEM irradiation was performed at the I^3TEM housed in the Ion Beam Laboratory at Sandia National Laboratories. The I^3TEM is a highly modified JEOL 2100 TEM operated at 200 kV with a port for ion beamlines perpendicular to the electron beam [78], enabling ion irradiation or implantation concurrent to

real-time TEM imaging. For this experiment, a 6 MV High-Voltage Engineering Europa Tandem accelerator was used to generate a 46 keV Au^- ion beam. A 25 nA beam was incident over a 0.20 cm^2 area on the TiO_2 nanotubes at ambient temperature. The beam flux was 7.7×10^{11} ions/cm^2 s and was maintained for ~ 5 min, to a total fluence of ~ 2.3×10^{14} ions/cm^2. Bright-field TEM videos were captured of individual nanotubes throughout the duration of in situ irradiation (~ few minutes).

Nuclear and electronic stopping powers were calculated as a function of incident Au^- ion energy for anatase TiO_2 (density 3.89 g/cm^3) using the "Stopping/Range Tables" module in Stopping and Range of Ions in Matter (SRIM) [79]. For 46 keV Au ions specifically, vacancy and ion implantation profiles were determined using SRIM in "Detailed Calculation with full Damage Cascades" mode based upon recent recommendations from Agarwal et al. [80] regarding the accuracy of this mode for calculating vacancy production. The displacement energies for Ti and O atoms in SRIM were set to the default values of 25 and 28 eV, respectively. A simulated anatase TiO_2 layer was created by setting the SRIM target density to 3.89 g/cm^3 [81]. For simulated amorphous TiO_2, the density was set to 2.43 g/cm^3. This value for the density is based on the following equation:

$$\rho_{amorph} = \rho_{ana}\left(\frac{V_{ana}}{V_{amorph}}\right) \qquad (4)$$

where ρ_{ana} is the density of anatase TiO_2, and V_{ana} and V_{amorph} are the molecular dynamics calculated unit cell volumes for anatase and amorphous TiO_2, respectively (see Sect. 5.3). Figure 7 provides the SRIM detailed calculation results for vacancy production and ion implantation; Figures S3 and S4 (Supplementary Information) are shown for a comparison of damage profiles across various SRIM calculation modes. The density difference between the amorphous and the anatase TiO_2 results in the vacancy production and ion implantation peaks being separated by ~ 100 Å.

Post-irradiation TEM characterization was used to provide information on the yielded morphology and structure. This work was conducted on a FEI Tecnai TF30 FEG TEM operated at 300 kV at the Microscopy and Characterization Suite (MaCS) in the Center for Advanced Energy Studies (CAES) as well as on a FEI Tecnai TF20 FEG TEM operated at 200 kV at Purdue University. The irradiated nanotubes were characterized using bright field TEM and HRTEM.

Molecular dynamics

Classical Molecular Dynamics (CMD) simulations were performed to compute the difference in volume between amorphous and anatase phases of TiO_2 using LAMMPS. A reactive force field (ReaxFF) was employed to describe the interactions between Ti and O atoms [82]. To assess the suitability

of ReaxFF for investigating TiO_2, we computed the cohesive energy and oxygen vacancy formation energy of anatase TiO_2. The O-vacancy formation energy E_v was calculated by the following equation:

$$E_v = E_{TiO_2,v} - E_{TiO_2} - \frac{E_{O_2}}{2}, \qquad (5)$$

where $E_{TiO_2,v}$ is the energy of a TiO_2 supercell containing 10 unit cells and one O-vacancy, E_{TiO_2} is the energy of pristine TiO_2 supercell containing 10 unit cells, and E_{O_2} is the binding energy of an isoloated O_2 molecule. The ReaxFF predictions for cohesive energy (9.08 eV/ TiO_2) and O-vacancy formation energy (5.12 eV/TiO_2) of anatase TiO_2 were close to those obtained from previous density functional theory calculations with hybrid screened exchange functional [83].

All CMD calculations were performed using LAMMPS [84] to compute the difference in volume between anatase and amorphous TiO_2 phases under ambient conditions. To construct a representative configuration for amorphous TiO_2, a computational supercell of anatase (55.67 nm × 47.09 nm × 26.89 nm, or 20,250 atoms) was prepared by replicating the unit cell (taken from Materials Project [85]) ten times along each lattice vector. Periodic boundary conditions were employed along all directions. Thereafter, the super cell was equilibrated at 5000 K for 200 ps with a time step of 1.0 fs, before quenching to 300 K at a cooling rate of 2.5×10^{13} K using isothermal-isobaric (NPT) ensemble. The amorphous configuration was equilibrated for an additional 100 ps at 300 K with a time step of 1.0 fs within the canonical ensemble. The radical distribution functions of the as-prepared amorphous structured were similar to previous reports. The volume was calculated using LAMMPS internal subroutines by multiplying the length of the box in each axis direction.

Data availability

All data generated or analyzed during this study are included in this published article (and its supplementary information files).

Declarations

Conflict of interest The authors declare that they have no conflict of interests.

Supplementary Information

The online version contains supplementary material available at https://doi.org/10.1557/s43578-022-00516-2.

References

1. O. Carp, C.L. Huisman, A. Reller, Photoinduced reactivity of titanium dioxide. Prog. Solid State Chem. **32**(1–2), 33–177 (2004)
2. U. Diebold, The surface science of titanium dioxide. Surf. Sci. Rep. **48**(5–8), 53–229 (2003)
3. A. Fujishima, K. Honda, Electrochemical photolysis of water at a semiconductor electrode. Nature **238**(5358), 37–38 (1972)
4. B.R. Weinberger, R.B. Garber, Titanium dioxide photocatalysts produced by reactive magnetron sputtering. Appl. Phys. Lett. **66**(18), 2409–2411 (1995)
5. J.H. Park, S. Kim, A.J. Bard, Novel carbon-doped TiO2 nanotube arrays with high aspect ratios for efficient solar water splitting. Nano Lett. **6**(1), 24–28 (2006)
6. Z. Zhang, C.-C. Wang, R. Zakaria, J.Y. Ying, Role of particle size in nanocrystalline TiO2-based photocatalysts. J. Phys. Chem. B **102**(52), 10871–10878 (1998)
7. H. Zhang, R. Lee Penn, R.J. Hamers, J.F. Banfield, Enhanced adsorption of molecules on surfaces of nanocrystalline particles. J. Phys. Chem. B **103**(22), 4656–4662 (1999)
8. H. Zhang, M. Finnegan, J.F. Banfield, Preparing single-phase nanocrystalline anatase from amorphous titania with particle sizes tailored by temperature. Nano Lett. **1**(2), 81–85 (2001)
9. C. Jiang, M. Wei, Z. Qi, T. Kudo, I. Honma, H. Zhou, Particle size dependence of the lithium storage capability and high rate performance of nanocrystalline anatase TiO2 electrode. J. Power Sources **166**(1), 239–243 (2007)
10. Z. Yang, D. Choi, S. Kerisit, K.M. Rosso, D. Wang, J. Zhang, G. Graff, J. Liu, Nanostructures and lithium electrochemical

reactivity of lithium titanites and titanium oxides: a review. J. Power Sources **192**(2), 588–598 (2009)

11. D. Guan, P.J. Hymel, Y. Wang, Growth mechanism and morphology control of double-layer and bamboo-type TiO2 nanotube arrays by anodic oxidation. Electrochim. Acta **83**, 420–429 (2012)

12. J.-H. Kim, K. Zhu, J.Y. Kim, A.J. Frank, Tailoring oriented TiO2 nanotube morphology for improved Li storage kinetics. Electrochim. Acta **88**, 123–128 (2013)

13. C. Adán, J. Marugán, E. Sánchez, C. Pablos, R. Van Grieken, Understanding the effect of morphology on the photocatalytic activity of TiO2 nanotube array electrodes. Electrochim. Acta **191**, 521–529 (2016)

14. S. Li, Y. Liu, G. Zhang, X. Zhao, J. Yin, The role of the TiO2 nanotube array morphologies in the dye-sensitized solar cells. Thin Solid Films **520**(2), 689–693 (2011)

15. C.-W. Wang, W.-D. Zhu, J.-B. Chen, X. Hou, X.-Q. Zhang, Y. Li, J. Wang, F. Zhou, Low-temperature ammonia annealed TiO2 nanotube arrays: synergy of morphology improvement and nitrogen doping for enhanced field emission. Thin Solid Films **556**, 440–446 (2014)

16. M. Kulkarni, A. Mazare, J. Park, E. Gongadze, M.S. Killian, S. Kralj, K. von der Mark, A. Iglič, P. Schmuki, Protein interactions with layers of TiO2 nanotube and nanopore arrays: morphology and surface charge influence. Acta Biomater. **45**, 357–366 (2016)

17. R.P. Antony, T. Mathews, S. Dash, A.K. Tyagi, B. Raj, X-ray photoelectron spectroscopic studies of anodically synthesized self aligned TiO2 nanotube arrays and the effect of electrochemical parameters on tube morphology. Mater. Chem. Phys. **132**(2–3), 957–966 (2012)

18. S.T. Nishanthi, E. Subramanian, B. Sundarakannan, D. Pathinettam Padiyan, An insight into the influence of morphology on the photoelectrochemical activity of TiO2 nanotube arrays. Solar Energy Mater. Solar Cells **132**, 204–209 (2015)

19. N.T. Nguyen, I. Hwang, T. Kondo, T. Yanagishita, H. Masuda, P. Schmuki, Optimizing TiO2 nanotube morphology for enhanced photocatalytic H2 evolution using single-walled and highly ordered TiO2 nanotubes decorated with dewetted Au nanoparticles. Electrochem. Commun. **79**, 46–50 (2017)

20. S.P. Albu, H. Tsuchiya, S. Fujimoto, P. Schmuki, TiO2 nanotubes–annealing effects on detailed morphology and structure. Eur. J. Inorg. Chem. **2010**(27), 4351–4356 (2010)

21. S. Berger, R. Hahn, P. Roy, P. Schmuki, Self-organized TiO2 nanotubes: factors affecting their morphology and properties. Phys. Status Solidi B **247**(10), 2424–2435 (2010)

22. D. Wang, L. Liu, Continuous fabrication of free-standing TiO2 nanotube array membranes with controllable morphology for depositing interdigitated heterojunctions. Chem. Mater. **22**(24), 6656–6664 (2010)

23. D. Wang, Y. Liu, Yu. Bo, F. Zhou, W. Liu, TiO2 nanotubes with tunable morphology, diameter, and length: synthesis and

photo-electrical/catalytic performance. Chem. Mater. **21**(7), 1198–1206 (2009)

24. K. Das, S. Bose, A. Bandyopadhyay, TiO2 nanotubes on Ti: Influence of nanoscale morphology on bone cell–materials interaction. J. Biomed. Materials Res. A **90**(1), 225–237 (2009)

25. D. Kim, A. Ghicov, S.P. Albu, P. Schmuki, Bamboo-type TiO2 nanotubes: improved conversion efficiency in dye-sensitized solar cells. J. Am. Chem. Soc. **130**(49), 16454–16455 (2008)

26. J. Yu, G. Dai, B. Cheng, Effect of crystallization methods on morphology and photocatalytic activity of anodized TiO2 nanotube array films. J. Phys. Chem. C **114**(45), 19378–19385 (2010)

27. X. Luan, D. Guan, Y. Wang, Facile synthesis and morphology control of bamboo-type TiO2 nanotube arrays for high-efficiency dye-sensitized solar cells. J. Phys. Chem. C **116**(27), 14257–14263 (2012)

28. T. Toyoda, Q. Shen, Quantum-dot-sensitized solar cells: effect of nanostructured TiO2 morphologies on photovoltaic properties. J. Phys. Chem. Lett. **3**(14), 1885–1893 (2012)

29. A.G. Kontos, A.I. Kontos, D.S. Tsoukleris, V. Likodimos, J. Kunze, P. Schmuki, P. Falaras, Photo-induced effects on self-organized TiO2 nanotube arrays: the influence of surface morphology. Nanotechnology **20**(4), 045603 (2008)

30. A. Nakahira, T. Kubo, C. Numako, Formation mechanism of TiO2-derived titanate nanotubes prepared by the hydrothermal process. Inorg. Chem. **49**(13), 5845–5852 (2010)

31. J.M. Macak, H. Tsuchiya, A. Ghicov, K. Yasuda, R. Hahn, S. Bauer, P. Schmuki, TiO2 nanotubes: Self-organized electrochemical formation, properties and applications. Curr. Opin. Solid State Mater. Sci. **11**(1–2), 3–18 (2007)

32. G. Was, *Fundamentals of Radiation Materials Science: Metals and Alloys*, 2nd edn. (Springer, New York, 2018)

33. B. Uberuaga, X. Bai, Defects in rutile and anatase polymorphs of Tio2: kinetics and thermodynamics near grain boundaries. J. Phys. **23**(43), 435004 (2011)

34. X. Bai, B. Uberuaga, The influence of grain boundaries on radiation-induced point defect production in materials: a review of atomistic studies. JOM **65**(3), 360–373 (2013)

35. K.A. Smith, A.I. Savva, K.S. Mao, Y. Wang, D.A. Tenne, D. Chen, Y. Liu et al., Effect of proton irradiation on anatase TiO2 nanotube anodes for lithium-ion batteries. J. Mater. Sci. **54**(20), 13221–13235 (2019)

36. K.A. Smith, A.I. Savva, C. Deng, J.P. Wharry, S. Hwang, D. Su, Y. Wang et al., Effects of proton irradiation on structural and electrochemical charge storage properties of TiO2 nanotube electrodes for lithium-ion batteries. J. Mater. Chem. A **5**(23), 11815–11824 (2017)

37. B.I. Kharisov, O.V. Kharissova, U.O. Méndez (eds.), *Radiation Synthesis of Materials and Compounds* (CRC Press, Boca Raton, 2016)

38. H.M. Kim, H.S. Kim, S.K. Park, J. Joo, T.J. Lee, C.J. Lee, Morphological change of multiwalled carbon nanotubes through

high-energy (MeV) ion irradiation. J Appl. Phys. **97**, 026103 (2005)

39. E. Rui, J. Yang, X. Li, C. Liu, Change of surface morphology and structure of multi-walled carbon nanotubes film caused by proton irradiation with 170 keV. Appl. Surf. Sci. **287**, 172–177 (2013)

40. A. Singh, R. Kumari, V. Kumar, L. Krishnia, Z. Naqvi, A.K. Panwar, U.M. Bhatta, A. Ghosh, P.V. Satyam, P.K. Tyagi, Electron irradiation induced buckling, morphological transformation, and inverse Ostwald ripening in nanorod filled inside carbon nanotube. Appl. Surf. Sci. **360**, 1003–1008 (2016)

41. M. Shirai, K. Tsumori, M. Kutsuwada, K. Yasuda, S. Matsumura, Morphological change in FePt nanogranular thin films induced by swift heavy ion irradiation. Nuclear Instrum Methods Phys Res B **267**(10), 1787–1791 (2009)

42. A.G. Perez-Bergquist, K. Li, Y. Zhang, L. Wang, Ion irradiation-induced bimodal surface morphology changes in InSb. Nanotechnology **21**(32), 325602 (2010)

43. J.P. Wharry, H.C. Xiong, T.O., C.Y., Radiation effects in battery materials, in *Reference Module in Earth Systems and Environmental Sciences* (Elsevier, 2021). https://doi.org/10.1016/B978-0-12-819723-3.00109-8

44. K.E. Sickafus, *Comprehensive Nuclear Materials* (Elsevier Ltd, 2012), p. 28.

45. S. Dey, J.W. Drazin, Y. Wang, J.A. Valdez, T.G. Holesinger, B.P. Uberuaga, R.H.R. Castro, Radiation tolerance of nanocrystalline ceramics: insights from Yttria Stabilized Zirconia. Sci. Rep. **5**(1), 1–9 (2015)

46. T.D. Shen, S. Feng, M. Tang, J.A. Valdez, Y. Wang, K.E. Sickafus, Enhanced radiation tolerance in nanocrystalline Mg Ga2O4. Appl. Phys. Lett. **90**(26), 263115 (2007)

47. A. Meldrum, L.A. Boatner, R.C. Ewing, Electron-irradiation-induced nucleation and growth in amorphous LaPO4, ScPO4, and zircon. J. Mater. Res. **12**(7), 1816–1827 (1997)

48. M. Libera, Local amorphous thin-film crystallization induced by focused electron-beam irradiation. Appl. Phys. Lett. **68**(3), 331–333 (1996)

49. W. Qin, T. Nagase, Y. Umakoshi, Electron irradiation-induced nanocrystallization of amorphous Fe85B15 alloy: evidence for athermal nature. Acta Mater. **57**(4), 1300–1307 (2009)

50. E. Akcöltekin, T. Peters, R. Meyer, A. Duvenbeck, M. Klusmann, I. Monnet, H. Lebius, M. Schleberger, Creation of multiple nanodots by single ions. Nat. Nanotechnol. **2**(5), 290–294 (2007)

51. W. Qin, J.A. Szpunar, Y. Umakoshi, Electron or ion irradiation-induced phase-change mechanism between amorphous and crystalline state. Acta Mater. **59**(5), 2221–2228 (2011)

52. K. Dyrbye, J. Bo, K. Pampus, B. Torp, Radiation-enhanced diffusion in amorphous Pd-Cu-Si. Phys. Rev. B **38**(13), 8562 (1988)

53. S. Bellini, A. Montone, M. Vittori-Antisari, Radiation-enhanced diffusion in amorphous Ni-Zr studied by in situ electron

irradiation in a transmission electron microscope. Phys. Rev. B **50**(14), 9803 (1994)

54. Y. Zhang, H. Xue, E. Zarkadoula, R. Sachan, C. Ostrouchov, P. Liu, X. Wang, S. Zhang, T.S. Wang, W.J. Weber, Coupled electronic and atomic effects on defect evolution in silicon carbide under ion irradiation. Curr. Opin. Solid State Mater. Sci. **21**(6), 285–298 (2017)

55. M. Toulemonde, Ch. Dufour, E. Paumier, Transient thermal process after a high-energy heavy-ion irradiation of amorphous metals and semiconductors. Phys. Rev. B **46**(22), 14362 (1992)

56. M. Toulemonde, C. Dufour, A. Meftah, E. Paumier, Transient thermal processes in heavy ion irradiation of crystalline inorganic insulators. Nuclear Instrum. Methods Phys. Res. B **166**, 903–912 (2000)

57. R.L. Fleischer, P.B. Price, R.M. Walker, Ion explosion spike mechanism for formation of charged-particle tracks in solids. J. Appl. Phys. **36**(11), 3645–3652 (1965)

58. R.E. Johnson, B.U.R. Sundqvist, A. Hedin, D. Fenyö, Sputtering by fast ions based on a sum of impulses. Phys. Rev. B **40**(1), 49 (1989)

59. F. Seitz, J.S. Koehler, Displacement of atoms during irradiation. Solid-State Phys. **2**, 307 (1956)

60. G. Rizza, A. Dunlop, G. Jaskierowicz, M. Kopcewicz, Nucl. Instrum Methods B **224**, 609–621 (2004)

61. G. Rizza, A. Dunlop, G. Jaskierowicz, M. Kopcewicz, J. Phys. Cond. Matter **16**, 1547 (2014)

62. C.M. Lopatin, T.L. Alford, V.B. Pizziconi, M. Kuan, T. Laursen, Ion-beam densification of hydroxyapatite thin films. Nucl. Instrum. Methods Phys. Res. Sect. B **145**(4), 522–531 (1998)

63. K. Meinander, K. Nordlund, Irradiation-induced densification of cluster-assembled thin films. Phys. Rev. B **79**(4), 045411 (2009)

64. D.R. Gomes, A.A. Turkin, D.I. Vainchtein, JTh.M. De Hosson, Size-dependent ion-induced densification of nanoporous gold. Scr. Mater. **164**, 17–20 (2019)

65. E. Snoeks, A. Polman, C.A. Volkert, Densification, anisotropic deformation, and plastic flow of SiO2 during MeV heavy ion irradiation. Appl. Phys. Lett. **65**(19), 2487–2489 (1994)

66. E.P. EerNisse, Compaction of ion-implanted fused silica. J. Appl. Phys. **45**(1), 167–174 (1974)

67. A. Wootton, B. Thomas, P. Harrowell, Radiation-induced densification in amorphous silica: a computer simulation study. J. Chem. Phys. **115**(7), 3336–3341 (2001)

68. S. Klaumünzer, Ion-beam-induced plastic deformation: a universal phenomenon in glasses. Radiat. Effects Defects Solids **110**(1–2), 79–83 (1989)

69. M. Ghaly, R.S. Averback, Effect of viscous flow on ion damage near solid surfaces. Phys. Rev. Lett. **72**(3), 364 (1994)

70. G. Buscarino, S. Agnello, F.M. Gelardi, Structural modifications induced by electron irradiation in SiO2 glass: local densification measurements. EPL (Europhysics Letters) **87**(2), 26007 (2009)

71. G. Buscarino, S. Agnello, F.M. Gelardi, R. Boscaino, The role of impurities in the irradiation induced densification of amorphous SiO2. J. Phys. **22**(25), 255403 (2010)

72. M. Mačković, F. Niekiel, L. Wondraczek, E. Spiecker, Direct observation of electron-beam-induced densification and hardening of silica nanoballs by in situ transmission electron microscopy and finite element method simulations. Acta Mater. **79**, 363–373 (2014)

73. M.D. Freshley, D.W. Brite, J.L. Daniel, P.E. Hart, Irradiation-induced densification of UO2 pellet fuel. J. Nucl. Mater. **62**(2–3), 138–166 (1976)

74. M.V. Speight, Point defects and irradiation-enhanced densification. Philos. Mag. **32**(6), 1101–1105 (1975)

75. I. Greenquist, M. Tonks, Y. Zhang, Analysis of the impact of fuel microstructure on irradiation-enhanced densification using grand potential simulations. Ann. Nucl. Energy **151**, 107858 (2021)

76. M.E. Cazado, A.C. Denis, Model of nuclear fuel pellets densification under irradiation and isothermal conditions: application to UO2 fuels. J. Nucl. Mater. **510**, 585–595 (2018)

77. P. Barnes, A. Savva, K. Dixon, H. Bull, L. Rill, D. Karsann, S. Croft, J. Schimpf, H. Xiong, Electropolishing valve metals with a sulfuric acid-methanol electrolyte at low temperature. Surf. Coat. Technol. **347**, 150–156 (2018)

78. K. Hattar, D.C. Bufford, D.L. Buller, Concurrent in situ ion irradiation transmission electron microscope. Nuclear Instrum. Methods Phys. Res. B **338**, 56–65 (2014)

79. J.F. Ziegler, M.D. Ziegler, J.P. Biersack, SRIM–The stopping and range of ions in matter. Nucl. Instrum. Methods Phys. Res. Sect. B **268**(11–12), 1818–1823 (2010)

80. S. Agarwal, Y. Lin, C. Li, R.E. Stoller, S.J. Zinkle, On the use of SRIM for calculating vacancy production: quick calculation and full-cascade options. Nucl. Instrum. Methods Phys. Res. Sect. B **503**, 11–29 (2021)

81. J. Anthony, *Handbook of Mineralogy (Volume III)* (Mineral Data Publ, Tuscon, Ariz, 1995)

82. S. Monti, V. Carravetta, H. Ågren, Simulation of gold functionalization with cysteine by reactive molecular dynamics. J. Phys. Chem. Lett. **7**(2), 272–276 (2016)

83. H. Li, Y. Guo, J. Robertson, Calculation of TiO2 surface and subsurface oxygen vacancy by the screened exchange functional. J. Phys. Chem. C **119**(32), 18160–18166 (2015)

84. A.P. Thompson, H.M. Aktulga, R. Berger, D.S. Bolintineanu, W.M. Brown, P.S. Crozier, P.J. Veld, A. Kohlmeyer, S.G. Moore, T.D. Nguyen, R. Shan, M.J. Stevens, J. Tranchida, C. Trott, S.J. Plimpton, LAMMPS—a flexible simulation tool for particle-based materials modeling at the atomic, meso, and continuum scales. Comput Phys Comm **271**(2022), 10817 (2022)

85. A. Jain, S.P. Ong, G. Hautier, W. Chen, W.D. Richards, S. Dacek, S. Cholia, D. Gunter, D. Skinner, G. Ceder, K.A. Persson, The materials project: a materials genome approach to accelerating materials innovation. APL Mater. **1**(1), 011002 (2013). https://doi.org/10.1063/1.4812323